Computers and Electronics in Agriculture 152 (2018) 90–100

Contents lists available at ScienceDirect

Computers and Electronics in Agriculture

journal homepage: www.elsevier.com/locate/compag

Original papers

Developing a system for three-dimensional quantification of root traits of rice seedlings

Tsung-Han Han, Yan-Fu Kuo*

Department of Bio-Industrial Mechatronics Engineering, National Taiwan University, Taipei, Taiwan

ARTICLE INFO

Keywords:
Root system architecture
Rice seedling root
Three-dimensional (3D) image
Convolutional neural network (CNN)

ABSTRACT

A plant's root system architecture (RSA) is the spatial configuration of its roots; the RSA of *Oryza sativa* L. (rice) shows a high degree of diversity. The RSA of rice should be quantified with high accuracy to understand the relationship between the RSA and functionality of rice roots. This study developed an imaging system for three-dimensional (3D) quantification of the RSA of rice. In this study, rice seedlings of 20 varieties were cultivated in glass tubes filled with transparent gellan gum for 10 days after germination. A servomotor-controlled camera captured two-dimensional side-view images of the seedlings at predetermined angles. A convolutional neural network classifier was then developed to segment the roots from the background. Subsequently, 3D images of the rice roots were constructed, and the phenotypic traits were quantified from the 3D images. Results displayed a high degree of diversity in the traits of the 20 varieties. A ground truth with designed parameters was used to validate the accuracy of this system. Analysis results indicated that the developed system was 98.3%, 97.6%, and 93.3% accurate regarding the primary root length, total root length, and root volume, respectively.

1. Introduction

Oryza sativa L. (rice) is one of the most widely consumed staple foods in the world. In recent years, rice cultivation has encountered many challenges, such as floods, droughts, and salinization of soil. The root system architectures (RSAs) of rice plants determine the nutrient absorption and water usage of those plants. Different varieties of rice exhibit high diversity among their RSAs (Fig. 1). The diversity in plant RSA has been considered to affect the physiological functionality of plants and is correlated with their fitness in the environment (Hinsinger et al., 2009; Hodge et al., 2009). Hence, it is essential to quantify the RSA of rice with high accuracy.

Previously, RSA and its functionality have mostly been studied using two-dimensional (2D) images. Armengaud et al. (2009) automated 2D imaging methods to measure the RSA traits of *Arabidopsis thaliana*. Clark et al. (2013) proposed a phenotyping system that quantified some RSA traits of rice seedlings by using digital images. Lobet et al. (2011) presented semi-automated image-analysis software to track the growth rates of the rice seedling roots by using time-lapse image sequences. Ao et al. (2010) compared the differences in root phenotypes between phosphorus-efficient and phosphorus-inefficient soybeans. Fenta et al. (2014) presented the variances in root phenotypes under drought tolerance for soybeans of different varieties. Another work developed a plant-root monitoring platform that recorded root growth over several days through video imaging (Yazdanbakhsh and Fisahn, 2009). Root architectures, however, have complex geometries. A considerable amount of information can be lost when root architectures are analyzed in terms of 2D images. Therefore, authentic 3D images must be acquired to retain the inherent architectural information of roots.

X-ray computed tomography (CT) has been shown as a powerful tool to examine the architecture of plant roots nondestructively. Heeraman et al. (1997) first used industrial X-ray CT to reconstruct 3D images of root networks. Jenneson et al. (1999) designed an X-ray CT system specifically for studying the development of plant roots in soil. Mairhofer et al. (2012) used visual-tracking techniques to enhance the image quality of X-ray CT systems. Pfeifer et al. (2015) presented algorithms to shorten the time for segmenting arbitrarily complex and unconnected root systems in X-ray CT images. Another study examined the interactions between roots and soil in-situ using X-ray micro-CT (Tracy et al., 2012). Although X-ray CT can be used for modeling root networks in very high precision, sophisticated instruments are required. The instruments are usually too costly or too difficult to be obtained.

Recent research has revealed that 3D root images of rice seedlings can be reconstructed using regular digital imaging (Clark et al., 2011; Zheng et al., 2011; Lopez et al., 2011; Topp et al., 2013). In these

---

* Corresponding author at: Department of Bio-Industrial Mechatronics Engineering, National Taiwan University, No. 1, Sec. 4, Roosevelt Rd., Taipei 106, Taiwan.
E-mail address: ykuo@ntu.edu.tw (Y.-F. Kuo).

https://doi.org/10.1016/j.compag.2018.07.001
Received 22 March 2018; Received in revised form 31 May 2018; Accepted 1 July 2018
0168-1699/

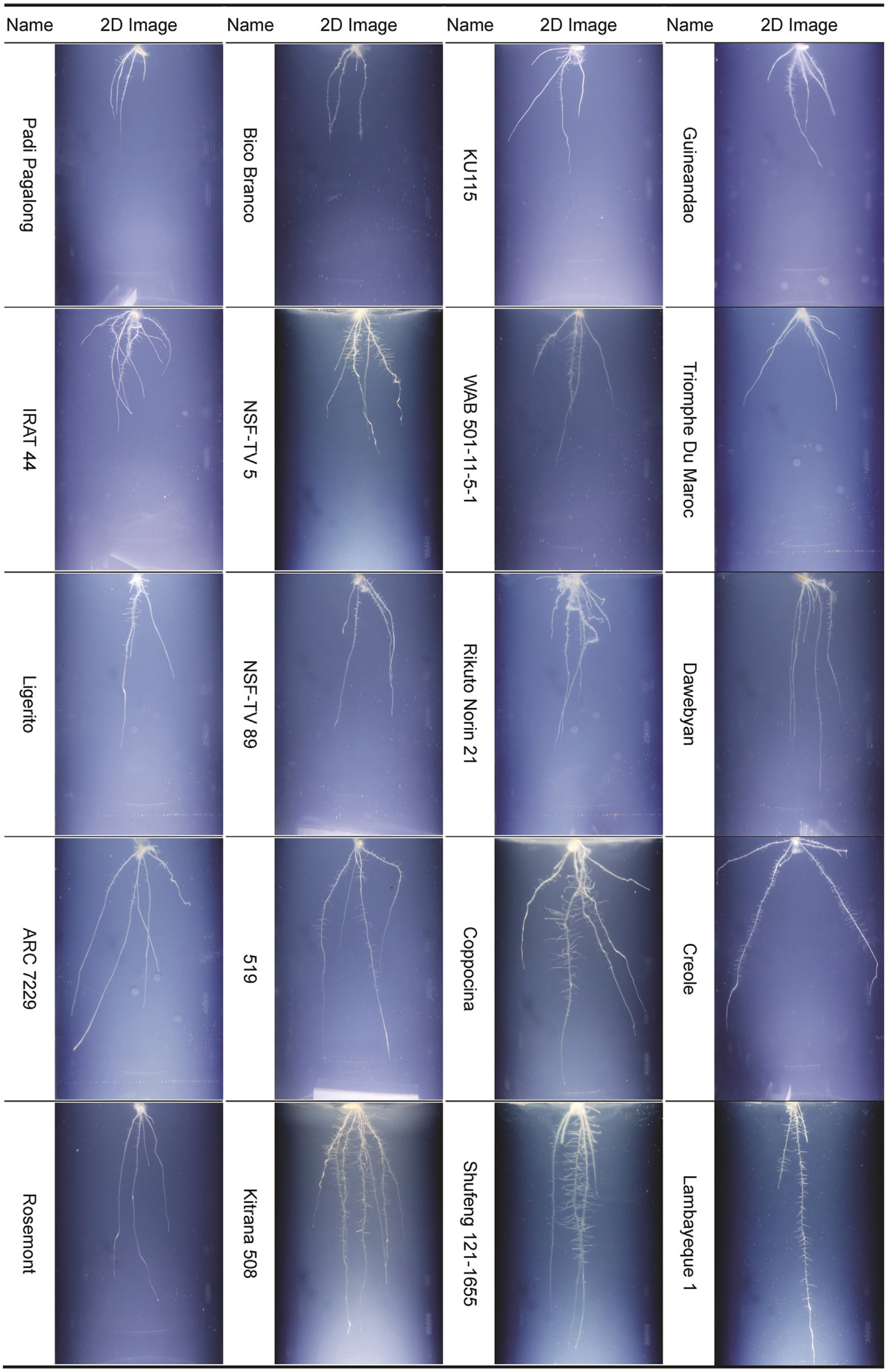

Fig. 1. Root images of 20 varieties of rice seedlings.

studies, rice seedlings were cultivated in a transparent gel medium. Three-dimensional root images of seedlings were then reconstructed from several 2D side-view images acquired at various angles using simple space carving (SSC; Kutulakos and Seitz, 2000). However, SSC is sensitive to noise. Redundant pixels (i.e., sparkles) and missing pixels in any 2D side-view image may cause false positive and false negative voxels in the 3D image, respectively. Thus, when reconstructing a root image in 3D, it is critical to accurately segment root parts from noise and background elements in the 2D side-view images.

In recent years, deep learning has emerged as a powerful tool for tackling complicated image segmentation problems (LeCun et al., 2015). Convolutional neural network (CNN; Krizhevsky et al., 2012) is one deep learning approach for image segmentation. Zhang et al. (2015) segmented infant brain tissues in magnetic resonance images at the isointense stage by using a CNN classifier. Ganin and Lempitsky (2014) presented an approach for natural edge detection in RGB images by using a CNN and nearest neighbor search. Another study combined a CNN and principal component analysis to segment retinas from blurred backgrounds (Wu et al., 2016). In this study, we improved the quality of rice root images presented in 3D by employing a CNN classifier for root segmentation.

This study conducted 3D quantification of RSA traits of rice seedlings for 20 varieties. The specific objectives of this study were to (1) cultivate rice seedlings of 20 varieties in glass tubes filled with a transparent gel medium, (2) develop an imaging platform for acquiring 2D side-view images of the seedling roots at predetermined angles, (3) apply a series of image processing algorithms and a CNN classifier for improving the quality of the side-view images, (4) reconstruct 3D images by using SSC and the side-view images, (5) quantify RSA traits from the 3D images, (6) present the morphological and physiological traits of the seedlings, and (7) validate the accuracy of the proposed system by employing a ground truth.

2. Materials and methods

2.1. Sample preparation

Rice seeds of 20 varieties were acquired from the Genetic Stocks Oryza germplasm collection (Agricultural Research Service, United States Department of Agriculture, USA; Table 1). The grain samples with NSFTV IDs of 5, 16, 86, 93, 96, 188, 315, 347, 364, 373, and 623 were prepared by Dr. Dong-Hong Wu, at the Agricultural Research Institute (Crop Science Division and Guansi Extension Station, Taiwan). The remaining grain samples were reproduced in a local greenhouse (Kaohsiung District Agricultural Research and Extension Station, Taiwan). The grains were dried to moisture content of approximately 13% and were stored in refrigerators at 4 °C. To prepare the seedlings, the rice hulls were removed for decreasing the risk of contamination during cultivation. The seeds were then soaked in bleaching solution (CLOROX, regular sodium hypochlorite packed at more than 6.25%) for 7 min and subsequently were soaked in ethyl alcohol solution (70%/volume) for 7 min. Subsequently, the seeds were rinsed approximately five times using reverse osmosis (RO) water to remove the solutions and were germinated in the dark by soaking the seeds in RO water added to sterile petri dishes for 3 days. The germination temperature was set to 30 °C. The pre-germinated seeds were cultivated in transparent glass tubes with gellan gum (Phytagel, Sigma-Aldrich; St. Louis, USA) as the growth medium (Fig. 2). To prepare the medium, 1.8-g Phytagel powder was dissolved in 1.25-L RO water and was autoclaved (STA-400, ST.FRANCIS; New Taipei, Taiwan) for 20 min at 121 °C. The solution was then mixed with 0.22 g $CaCl_2 \cdot 2H_2O$ and 0.21 g $MgSO_4 \cdot 7H_2O$ to solidify the medium. To emulate the dark growing condition in soil, the surfaces of the sterilized mediums in the glass tubes were covered using aluminum foil. Black cloths were used to wrap the glass tubes. The rice seedlings were cultivated in growth chambers for 10 days. The environment of the chambers was set to 25 °C with a day period of 12 h. Five replicates were cultivated for each variety, resulting a total of 100 seedlings.

Table 1
Varieties of rice seedlings.

Name	GSOR#	NSFTV ID	Sub-population	Country of origin
NSF-TV 5	301005	5	AROMATIC	India
ARC 7229	301006	6	AUS	India
Bico Branco	301014	16	AROMATIC	Brazil
NSF-TV 89	301081	89	TRJ	Thailand
Kitrana 508	301085	93	AROMATIC	Madagascar
KU115	301088	96	ADMIX	Thailand
Coppocina	301179	188	TRJ	Bulgaria
IRAT 44	301217	226	TRJ	Burkina Faso
WAB 501-11-5-1	301230	240	TRJ	Cote D'Ivoire
Guineandao	301243	253	ADMIX	Guinea
Padi Pagalong	301264	274	TRJ	Malaysia
Triomphe Du Maroc	301272	282	TEJ	Morocco
519	301294	304	IND	Uruguay
Dawebyan	301305	315	IND	Myanmar
Creole	301337	347	TRJ	Belize
Ligerito	301340	350	TRJ	Colombia
Rikuto Norin 21	301351	364	ADMIX	Japan
Lambayeque 1	301360	373	AROMATIC	Peru
Rosemont	301405	619	TRJ	United States
Shufeng 121-1655	301407	623	IND	China

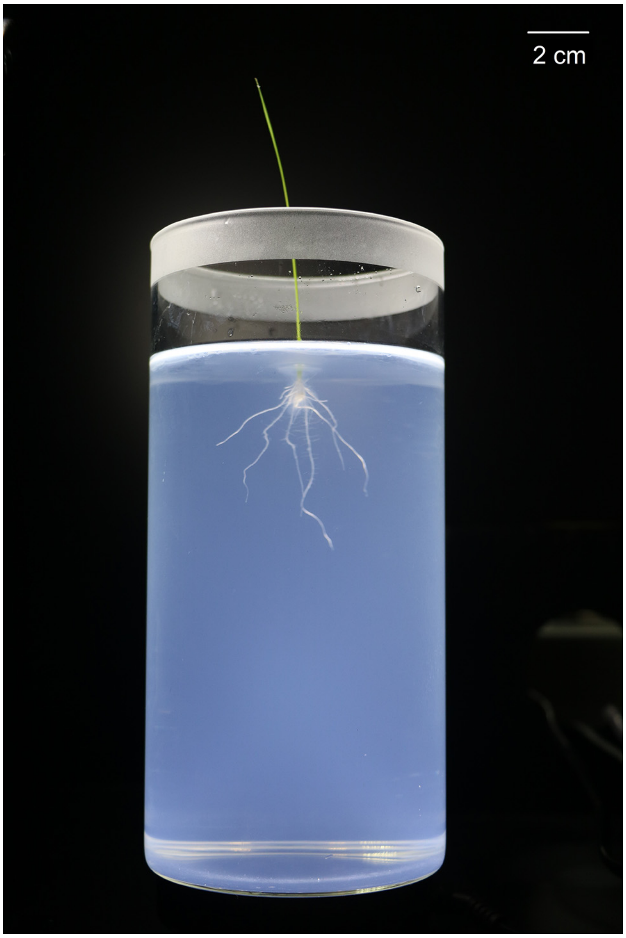

Fig. 2. Glass tube for seedling cultivation.

2.2. Imaging system development

An imaging system was developed to acquire 2D side-view images of the roots (Fig. 3). The system comprised a digital camera (EOS 760D, Canon, Tokyo, Japan), a servomotor (SLIM7-3909, CSIM, New Taipei, Taiwan), a connector with a mirror, a glass tube containing a seedling, a transparent water tank, an adjustable horizontal stand, and an LED illuminator (Fig. 3). The servomotor was mounted on the stand above the water tank. The connector was used to mount the glass tube on the servomotor. The illuminator was used to illuminate the seedlings during image acquisition. The mirror was fixed inside the connecter to reflect the light provided by the illuminator, thus creating a more uniform illumination. The water tank was filled with water to minimize the refraction due to the glass tubes. The camera was fixed on the stand beside the water tank to acquire side-view images of the seedling roots.

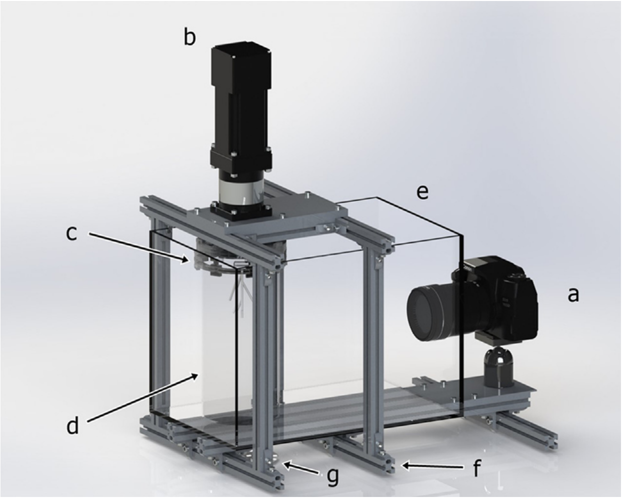

Fig. 3. Schematic of the imaging system: (a) digital camera, (b) servomotor, (c) connecter, (d) glass tube containing phytagel and the rice seedling, (e) water tank, (f) adjustable horizontal stand, and (g) LED illuminator.

The lens of the camera was set against the water tank to prevent refraction. The stand and camera were adjusted to a suitable level before image acquisition. The system was placed inside a dark chamber to avoid exposure to stray light.

To acquire the side-view root images, a glass tube containing a rice seedling was mounted on the servomotor. The servomotor and camera were connected to a computer and were controlled by a program developed using MATLAB (The MathWorks Inc., Natick, USA). The program controlled the servomotor to rotate the glass tubes and synchronously caused the camera to acquire images such that the side-view photographs of the roots were obtained at predetermined angles. A total of 36 photographs were acquired at 10° intervals in a range from 10° to 360°. Before the image acquisition for each specimen, the motor rotor was reset to zero, and the camera was set to the manual mode. The images were acquired using an ISO of 200, a focal length of 18 mm, an f-stop of 1/4.5, and a shutter speed of 0.25 s. The images were 6000 × 4000 pixels in size.

2.3. Background removal using a CNN

A series of algorithms were used to separate root networks and the background. A side-view image was first segmented into several overlapping patches by using a sliding window from the top-left corner to the bottom-right corner of the images (Fig. 4a). The size of the window was 50 × 50 pixels and the stride size was 10 pixels. A CNN classifier (Fig. 4c) was used to identify the patches containing any portion of the root network. The patches of 50 × 50 pixels were fed as input to the classifier (Fig. 4b). The outputs of the classifier were two classes – root patch and nonroot patch (Fig. 4d). The CNN classifier comprised five layers – two convolutional layers C_1 and C_2, one max pooling layer S_1, one flattened layer F_1, and one fully connected layer FC_1 (Fig. 4c). Layer C_1 accumulated the input patches into 32 feature maps of 50 × 50 pixels by using 3 × 3 pixel filters with a stride of 1 pixel. Moreover, layer S_1 performed nonlinear down-sampling on the feature maps of C_1 by using a 2 × 2 pixel filter with a stride of 1 pixel. Layer C_2 accumulated the feature maps of S_1 into 64 feature maps of 25 × 25 pixels by using 3 × 3 pixel filters with a stride of 1 pixel. The resulting feature maps were flattened into a sequence of 128 neurons. These neurons were fully connected to the two outputs. The activation function was a rectified linear unit (ReLU; Nair and Hinton, 2010), and the optimization algorithm adopted was Adam (Kingma and Ba, 2014). The model was trained using 300 root and 300 nonroot patches for 100 epochs. A graphic processing unit (GTX 1080, NVIDIA; Santa Clara, USA) was used to increase the training speed of the CNN classifier. Once a patch had been identified as a root patch (Fig. 4d) by the developed CNN classifier, the patch was binarized using Otsu's thresholding method (Otsu, 1979). The resulting binary patches of the same root image were then put together to form a silhouette.

2.4. Root model reconstruction in 3D

The 3D image of a root network was reconstructed using the generated silhouettes and SSC. SSC constructs the 3D image of a root network by projecting the pixels in the silhouettes back to a lump of

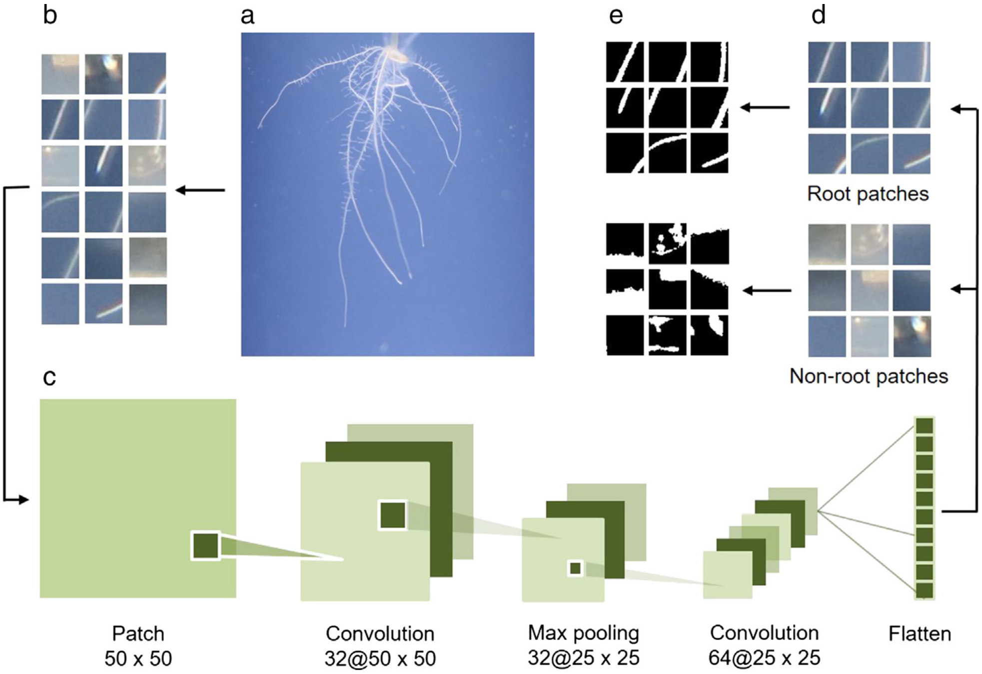

Fig. 4. Flowchart of the root silhouette generation. (a) A side-view image of a root network, (b) patches generated from a side-view image, (c) the CNN classifier, (d) root patches and nonroot patches classified by the CNN classifier, and (e) binarized patches.

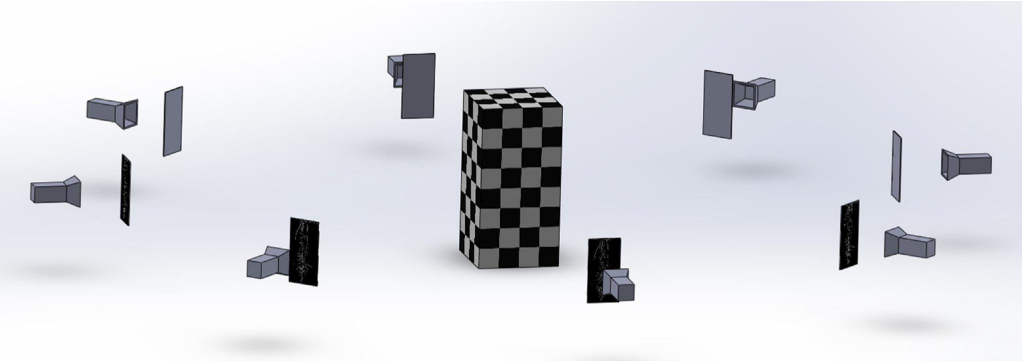

Fig. 5. Schematic for simple space carving.

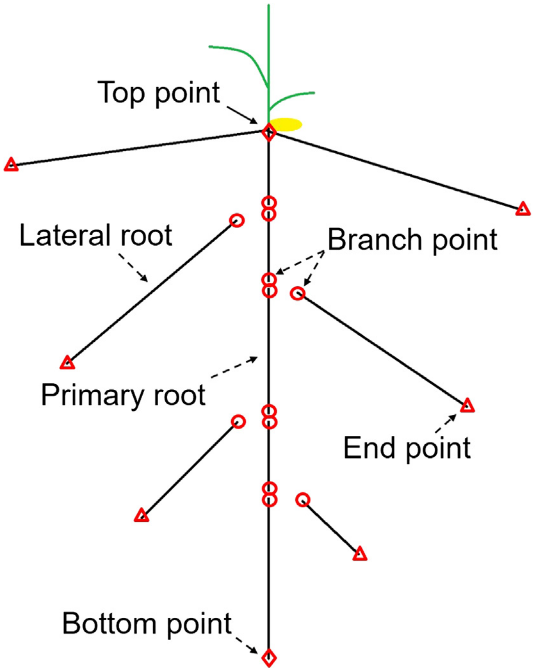

Fig. 6. Schematic of the root network skeleton. ○: branch points; □: end points; and ◇: top or bottom points.

clay that comprises 3D voxels. The voxels that are not part of the root network were then removed. The remaining voxels present the root network in 3D. The projection of a 2D pixel $x \in \mathbb{R}^{3\times1}$ in a silhouette to the corresponding 3D voxel $X_{3D} \in \mathbb{R}^{4\times1}$ in clay can be described as follows:

$$x = K[R|t]X_{3D} \tag{1}$$

where $K \in \mathbb{R}^{3\times3}$ is the matrix of intrinsic camera parameters, $R \in \mathbb{R}^{3\times3}$ is the orientation matrix of the camera, and $t \in \mathbb{R}^{3\times1}$ is the position matrix of the camera.

During the 3D model reconstruction, a solid voxel box was prepared as a lump of clay for carving. The voxel box was set at the center, and the silhouettes of the root network were placed around the voxel box at 10° intervals (Fig. 5). The silhouettes were then projected on the voxel box for removing the nonroot voxels by using Eq. (1). The calculation of Eq. (1) was conducted for all the voxels in the voxel box. Subsequently, the remaining voxels in the voxel box formed a 3D binary image of the root network.

2.5. Trait quantification

A root network comprises a primary (i.e., radical) root and lateral roots (Fig. 6; Ingram and Malamy, 2010). The primary root is the first root that emerges from a germinating seed and is the longest root in the seedling stage. The primary root branches to form lateral roots while growing. To identify the roots, branch points and end points of the root network were recognized. In the identification process, the binary skeleton image of the root network was obtained using 3D thinning (Lee

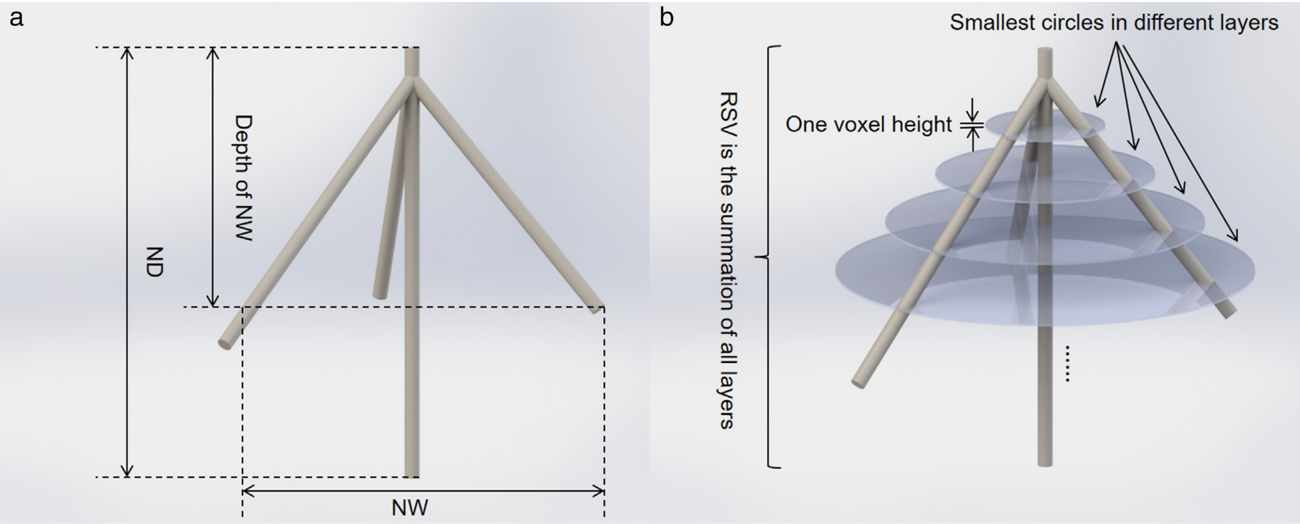

Fig. 7. Definitions of (a) ND, NW, and the depth of the NW horizon and (b) RSV.

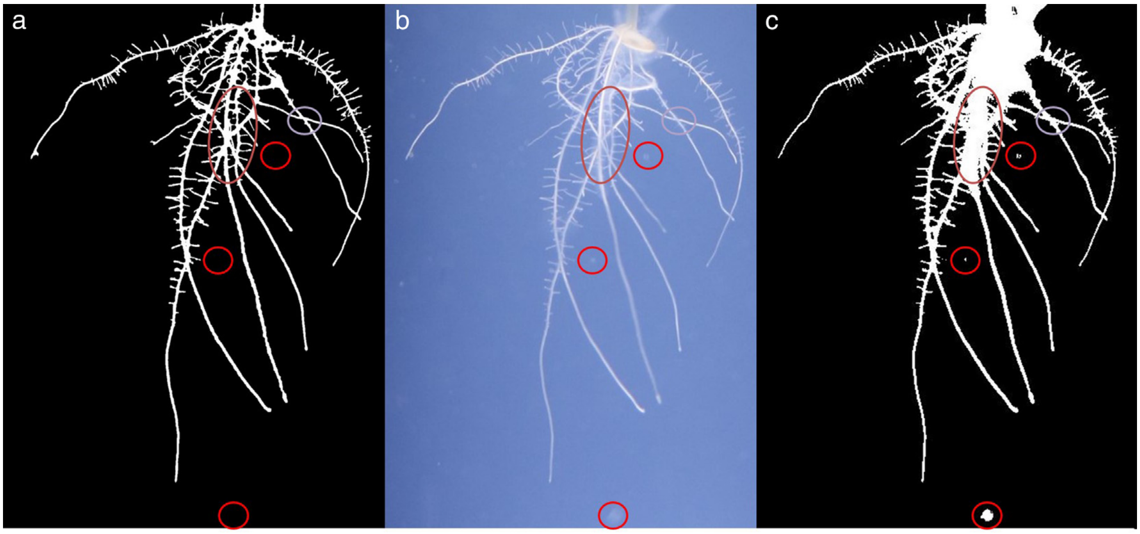

Fig. 8. (a) Silhouette generated using the proposed method, (b) side-view image of a root network, and (c) silhouette generated using the conventional Otsu method.

et al., 1994). The connectivity of all the voxels in the skeleton were calculated. The voxels with only one connected neighbor were labeled as end points. Moreover, the voxels with more than two connected neighbors were labeled as branch points. Subsequently, the skeleton image was separated into segments at the branch points (Fig. 6). The topmost and bottommost end points were marked as the top and bottom points, respectively. The shortest path comprising segments connecting the top and bottom points was defined as the primary root and was identified using Dijkstra's algorithm (Dijkstra, 1959). The paths connecting the branch points on the primary root to the end points were defined as lateral roots. The identified roots were used for trait quantification.

Ten RSA traits were quantified from the 3D models: total root length (TRL, mm), primary root length (PRL, mm), number of lateral roots (NLR, count), root surface area (SA, mm^2), root volume (RV, mm^3), network depth (ND, mm), network width (NW, mm), reachable soil volume (RSV, mm^3), structure aspect ratio (AR), and structure depth ratio (DR). ND was defined as the maximum vertical distance between two end points. NW was defined as the largest distance between two points on the root network in the same horizon level (Fig. 7a). RSV was defined as the volume of soil surrounding the root network. To calculate RSV, a 3D image was sliced into layers. The height of one layer was equal to the length of a voxel from the top point to the bottom point. For each layer, the smallest circle that encompassed the voxels was calculated. The summation of the smallest circles of all the layers was RSV (Fig. 7b). AR was defined as the ratio of NW to ND. DR was defined as the ratio of the depth of the NW horizon to ND (Fig. 7a).

2.6. Accuracy validation

The accuracy and resolution of the proposed system was validated using two hand-made root models with known parameters as the ground truths. The ground truths were made of copper wire with a diameter of 1 mm. One ground truth, referred to as simple ground truth, had a structure with straight lateral roots. The other ground truth, referred to as complex ground truth, had a structure with curled lateral roots. The PRL, TRL, and RV of the simple ground truth were 120 mm, 450 mm, and 353.43 mm^3, respectively. The PRL, TRL, and RV of the complex ground truth were 130 mm, 970 mm, and 761.84 mm^3, respectively. The 3D image and RSA traits of the ground truths were reconstructed and quantified using the proposed system. The quantified RSA traits were compared with the designed parameters to validate the accuracy of the system.

3. Results and discussion

3.1. 2D side-view images

Fig. 1 displays the side-view images of the roots for the 20 varieties of rice. The figure reveals that there was a high degree of diversity in the RSAs of the varieties. Moreover, the figures display considerable nonuniformity in illumination. An LED illuminator and a mirror were placed at the bottom and top of the tube, respectively (Fig. 3). Hence, the upper and lower halves of the images were usually brighter than the middle region. The nonuniformity complicated the segmentation of the roots from the background. This observation confirms the necessity of applying the proposed CNN method for background removal.

3.2. Images after background removal

The performance of the developed CNN classifier was verified using a test dataset comprising 300 root and 300 nonroot patches. The classifier was 95.1% accurate. When the sliding window scanned through a side-view image, all pixels were examined five times. Hence, the probability of misclassifying a root pixel as a nonroot pixel was 3.125×10^{-5}%.

Fig. 8 displays the silhouettes generated using the proposed method and the conventional Otsu's method. The figure reveals that the proposed method outperformed the conventional method. Noise elements in the side-view image were incorrectly recognized as root pixels, denoted as red circles, when the conventional method was employed. More fine details of the root network, represented as orange circles, were maintained when the proposed method was used. Moreover, the silhouette generated using the proposed method more clearly displayed the crossing at the root part, represented as yellow circles.

3.3. 3D root models

Fig. 9 displays the 3D root models of the 20 varieties reconstructed using the proposed method. The colors represent the depth. In general, the 3D models were able to represent the roots appropriately (Fig. 1). A high degree of diversity was observed in the RSAs of the varieties. Some varieties had a large depth (e.g., 519, Lambayeque 1, and Shufeng 121-1655), whereas some other varieties had a small depth (e.g., Bico Branco and Padi Pagalong). Some varieties had more lateral roots (e.g., Kitrana 508, Coppocina, and Shufeng 121-1655), whereas some other varieties barely had lateral roots (e.g., Bico Branco, NSF-TV 89, Padi Pagalong, and Triomphe Du Maroc). Some varieties had a centralized

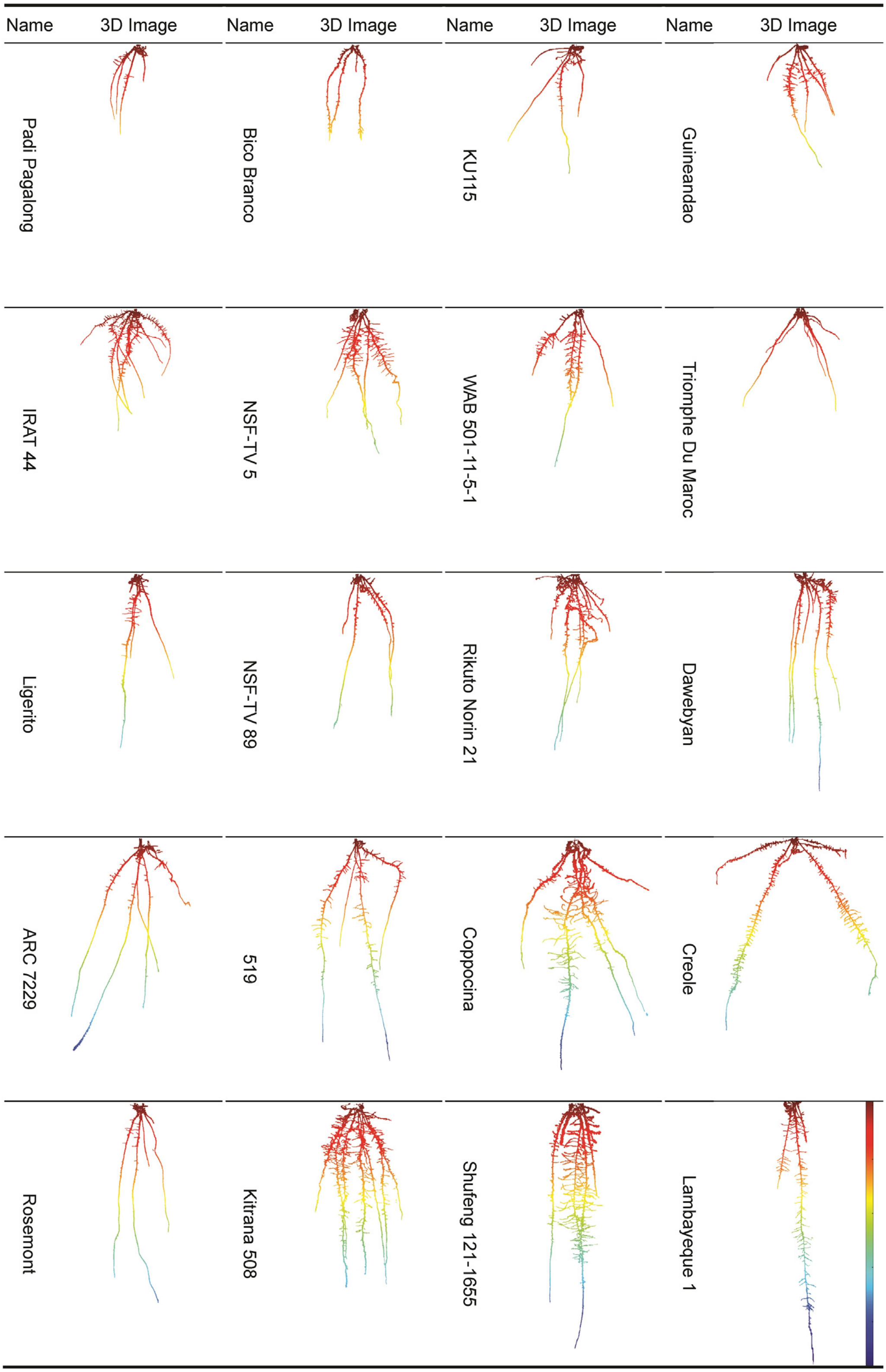

Fig. 9. 3D models of the seedling roots for the 20 varieties.

distribution (e.g., NSF-TV 5, Rikuto Norin 21, and Shufeng 121-1655), whereas some other varieties had dispersed distribution (e.g., Triomphe Du Maroc and Creole).

3.4. *Traits of the seedling roots*

Fig. 10 displays the boxplots of the ten traits. Five replicates per genotype was processed. High levels of variation were observed in the traits of the varieties. The means and standard deviations of the traits for all the seedlings were 361.94 ± 237.57 mm for TRL,

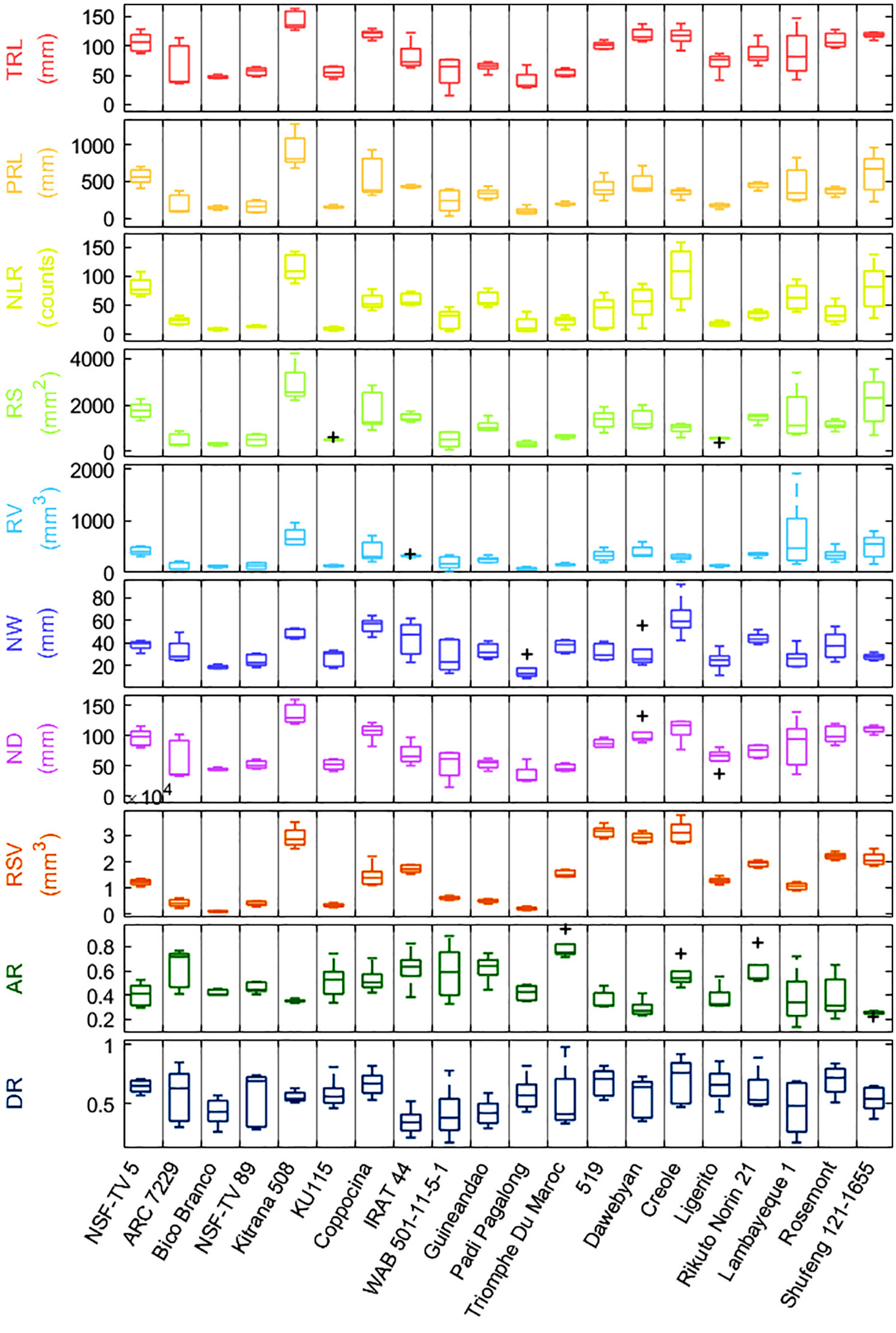

Fig. 10. RSA trait boxplots of the 20 varieties. TRL: total root length, PRL: primary root length, NLR: number of lateral roots, SA: root surface area; RV: root volume, NW: network width, ND: network depth, RSV: reachable soil volume, AR: structure aspect ratio, and DR: depth ratio.

85.15 ± 33.79 mm for PRL, 45.17 ± 35.96 units for NLR, 1143.55 ± 814.74 mm^2 for SA, 304.07 ± 249.62 mm^3 for RV, 34.34 ± 14.44 mm for NW, 77.22 ± 31.76 mm for ND, 14681.27 ± 10086.15 for RSV, 0.48 ± 0.17 for AR, and 0.56 ± 0.18 for DR. The differences between the traits of the varieties were significant (ANOVA; p value < 0.001).

Fig. 10 reveals that the trait values of Kitrana 508 were the highest except for the values of NW, AR, and DR. By contrast, the trait values of Bico Branco and Padi Pagalong were the smallest for almost all traits. Furthermore, ARC 7229, Kitriana 508, WAB 501-11-5-1, Creole, Lambayeque 1, and Shufeng 121-1655 displayed a relatively high level of within-variety variation in some traits (e.g., TRL, PRL, and ND). This observation implies that, for these varieties, the RSA development could strongly depend on environmental or some other extrinsic conditions, and the within-variety genotype variation of these varieties could be large.

3.5. Morphological variation in RSA

AR and DR were examined for the 20 varieties (Fig. 11). In the analysis, the distributions of AR and DR were presented for the 20 varieties using ellipsoids. Each ellipsoid was centered at the means of

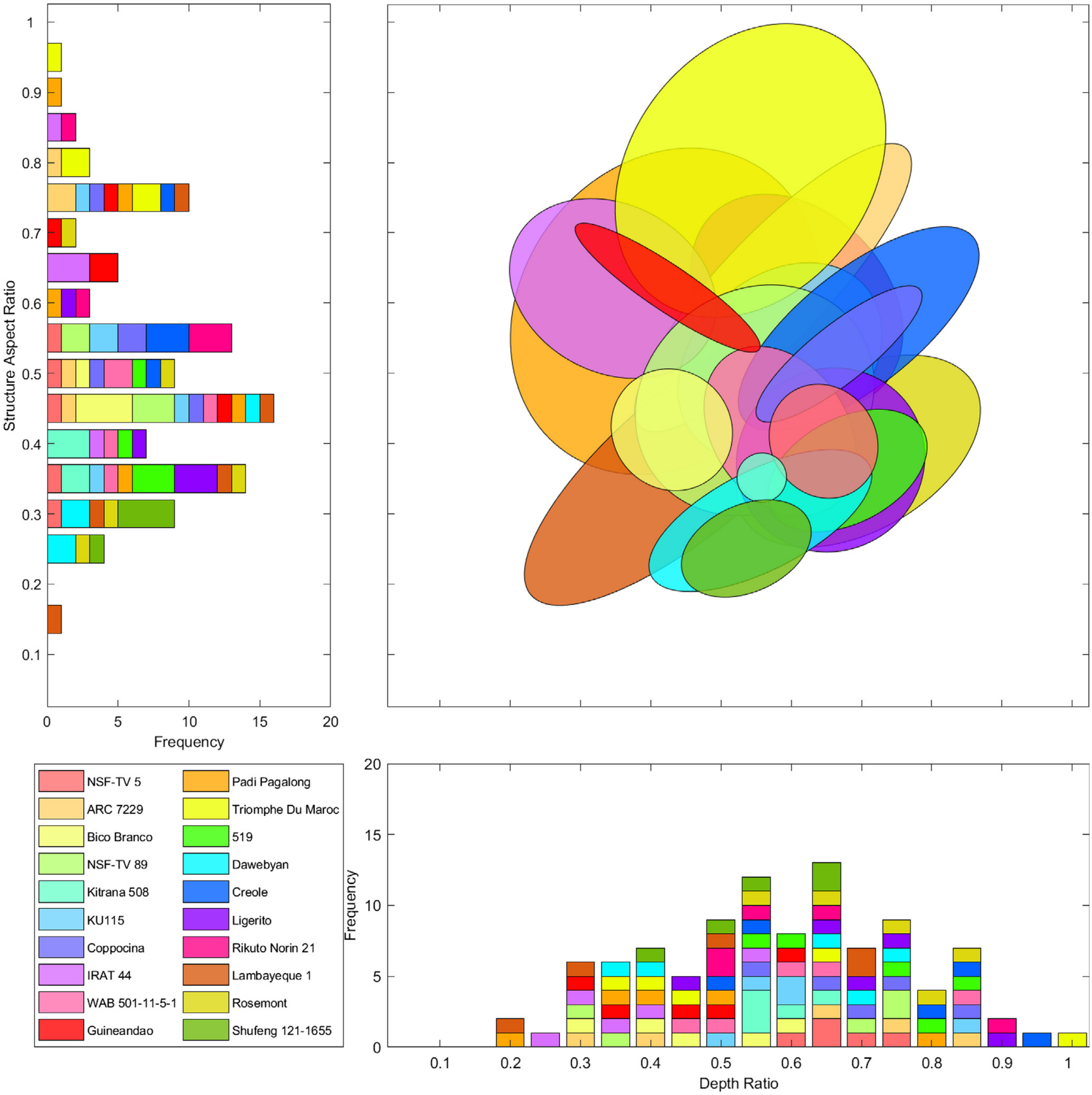

Fig. 11. Distribution of AR and DR for the 20 varieties.

the AR and DR parameters of the relevant variety. The principal axes of the ellipsoid were set parallel to the principal components (PCs) obtained by conducting a principal component analysis on the parameters. The lengths of the principal axes of the ellipsoid were set to two standard deviations of the PCs. The larger the AR was, the wider the root network was. The larger the DR was, the deeper the lateral roots grew.

Fig. 11 displays that Bico Branco, NSF-TV 89, and Shufeng 121-1655 had narrow AR distributions. Thus, each of these varieties may have a high degree of similarity in the seedling root appearance. By contrast, KU115, Padi Pagalong, Ligerito, and Lambayeque 1 had large variances for both AR and DR. The seedling roots for each of these varieties may be very different in appearance.

3.6. Functional variation in RSA

The primary function of roots is to absorb water and nutrients. The SA and RSV of a root network were considered to be correlated to the absorption efficiency of the root network and the amount of nutrients that can be obtained by the root network, respectively (Garrigues et al., 2006). Fig. 12 displays the mean values of SA and RSV for each variety. The figure indicates that SA and RSV for the varieties were not strongly correlated ($r^2 = 0.253$). Varieties such as NSF-TV 5, Lambayeque 1, and Coppocina had a high value of SA but a small value of RSV. By contrast, varieties such as Dawebyan, 519, and Creole had a large value of RSV but a small value of SA. This observation indicates that the morphological variation of the varieties may cause discrepancies in their physiological performance.

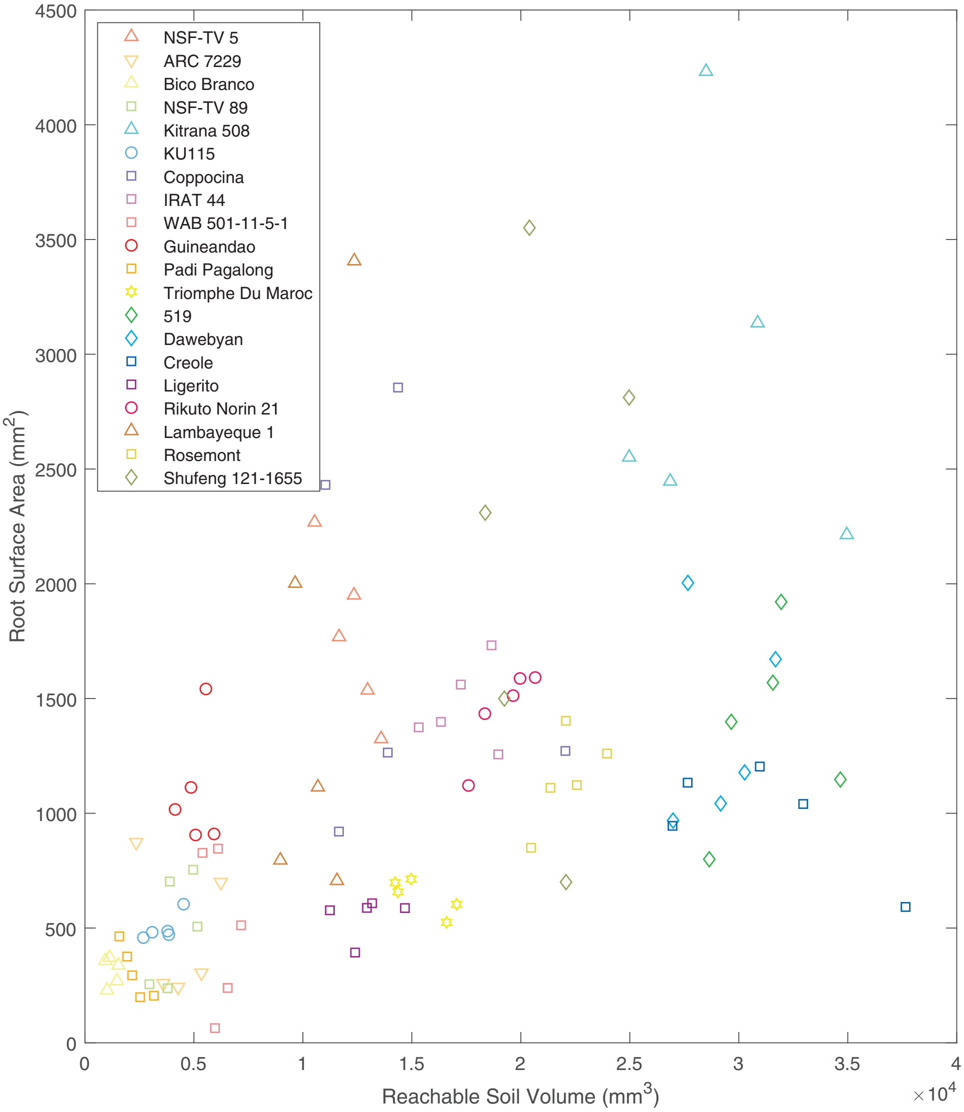

Fig. 12. Relationship between the SA and RSV values for all varieties. The color and shape of the edge plots present the variety and sub-population, respectively.

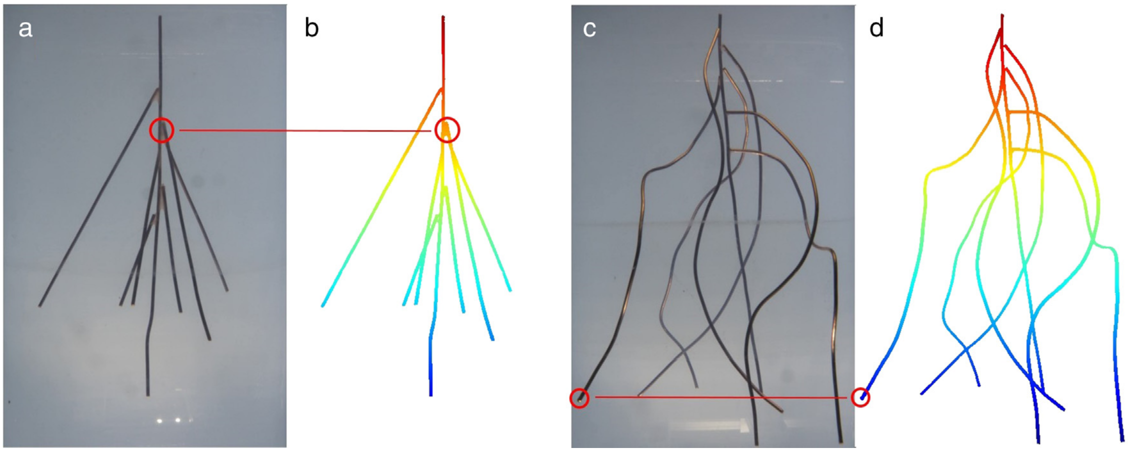

Fig. 13. The (a) photo and (b) reconstructed 3D image of the simple ground truth, and the (c) photo and (d) reconstructed 3D image of the complex ground truth.

3.7. Accuracy of the developed system

The 3D images of the ground truths were reconstructed using the proposed system (Fig. 13). The PRL, TRL, and RV quantified from the 3D image of the simple ground truth (Fig. 13b) were 117.21 mm, 473.17 mm, and 372.49 mm^3, respectively. The PRL, TRL, and RV quantified from the 3D image of the complex ground truth (Fig. 13d) were 128.45 mm, 981.57 mm, and 819.11 mm^3, respectively. The quantified traits were compared with the known parameters of the ground truths; the average accuracy of proposed system was 98.3% in estimating PRL, 97.6% in estimating TRL, and 93.3% in estimating RV.

Discrepancies between the hand-made root model and 3D image were observed. Shrinking and protruding was observed at the end points and branches of the roots (red circles displayed in Fig. 13). In the proposed system, the discrepancies were caused because the photographs were not taken at sufficiently small intervals. The defects can be diminished by reducing the photograph-taking interval (10° in this work). However, increasing the photograph-taking interval increases the time required for acquiring the side-view images and for reconstructing the 3D models. The thickness level of typical roots of rice seedlings is not as high as that of the ground truth (Fig. 1). The photograph-taking interval considered in this study may be adequate for providing a sufficient resolution for reconstructing the root structures of 10-day old rice seedlings.

4. Conclusion

This work proposed a system for quantifying traits of rice seedling roots in 3D. Rice seedlings from 20 cultivars were cultivated in transparent glass tubes and gellan gum. A customized imaging system and a CNN classifier were used to acquire 2D side-view images of the seedling roots and to convert the images to silhouettes, respectively. SSC technique was subsequently performed to reconstruct 3D models of the seedling roots by using the silhouettes. The traits quantified from the 3D models indicated that high degrees of diversity in both root morphology and function between the varieties. Analysis results indicated that the developed system reached accuracies of 98.3% for estimating PRL, 97.6% for estimating TRL and 93.3% for estimating RV.

Acknowledgments

This research was supported by the National Science Council (The Ministry of Science and Technology), Taiwan, by the grant provided to Yan-Fu Kuo; grant number: MOST 104-2311-B-002-019-MY3. We thank Dr. Chia-Lin Chung and Dr. Ruey-Fen Liou, National Taiwan University, Taiwan, for providing the rice samples and instruments used in this research.

Appendix A. Supplementary material

Supplementary data associated with this article can be found, in the online version, at https://doi.org/10.1016/j.compag.2018.07.001.

References

Ao, J., Fu, J., Tian, J., Yan, X., Liao, H., 2010. Genetic variability for root morph-architecture traits and root growth dynamics as related to phosphorus efficiency in soybean. Funct. Plant Biol. 37 (4), 304–312.

Armengaud, P., Zambaux, K., Hills, A., Sulpice, R., Pattison, R.J., Blatt, M.R., Amtmann, A., 2009. EZ-Rhizo: integrated software for the fast and accurate measurement of root system architecture. Plant Journal 57 (5), 945–956.

Clark, R.T., MacCurdy, R.B., Jung, J.K., Shaff, J.E., McCouch, S.R., Aneshansley, D.J., Kochian, L.V., 2011. Three-dimensional root phenotyping with a novel imaging and software platform. Plant Physiol. 156 (2), 455–465.

Clark, R.T., Famoso, A.N., Zhao, K.Y., Shaff, J.E., Craft, E.J., Bustamante, C.D., Kochian, L.V., 2013. High-throughput two-dimensional root system phenotyping platform facilitates genetic analysis of root growth and development. Plant, Cell Environ. 36 (2), 454–466.

Dijkstra, E.W., 1959. A note on two problems in connexion with graphs. Numerische mathematik 1 (1), 269–271.

Fenta, B.A., Beebe, S.E., Kunert, K.J., Burridge, J.D., Barlow, K.M., Lynch, J.P., Foyer, C.H., 2014. Field phenotyping of soybean roots for drought stress tolerance. Agronomy 4 (3), 418–435.

Ganin, Y., Lempitsky, V., 2014. N^ 4-Fields: Neural Network Nearest Neighbor Fields for Image Transforms. In: Asian Conference on Computer Vision. Springer, Cham, pp. 536–551.

Garrigues, E., Doussan, C., Pierret, A., 2006. Water uptake by plant roots: I-Formation and propagation of a water extraction front in mature root systems as evidenced by 2D light transmission imaging. Plant Soil 283 (1–2), 83.

Heeraman, D.A., Hopmans, J.W., Clausnitzer, V., 1997. Three dimensional imaging of plant roots in situ with X-ray computed tomography. Plant Soil 189 (2), 167–179.

Hinsinger, P., Bengough, A.G., Vetterlein, D., Young, I.M., 2009. Rhizosphere: biophysics, biogeochemistry and ecological relevance. Plant Soil 321 (1–2), 117–152.

Hodge, A., Berta, G., Doussan, C., Merchan, F., Crespi, M., 2009. Plant root growth, architecture and function. Plant Soil 321 (1–2), 153–187.

Ingram, P.A., Malamy, J.E., 2010. Root system architecture. Adv. Bot. Res. 55, 75–117 Academic Press.

Jenneson, P.M., Gilboy, W.B., Morton, E.J., Luggar, R.D., Gregory, P.J., Hutchinson, D., 1999. Optimisation of X-ray micro-tomography for the in situ study of the development of plant roots. In: Conference Record .1999 IEEE, Nuclear Science Symposium, vol. 1. IEEE, pp. 429–432.

Kingma, D.P., Ba, J., 2014. Adam: A method for stochastic optimization. arXiv preprint arXiv:1412.6980.

Krizhevsky, A., Sutskever, I., Hinton, G.E., 2012. Imagenet classification with deep convolutional neural networks. Adv. Neural Inform. Process. Syst. 1097–1105.

Kutulakos, K.N., Seitz, S.M., 2000. A theory of shape by space carving. Int. J. Comput. Vision 38 (3), 199–218.

LeCun, Y., Bengio, Y., Hinton, G., 2015. Deep learning. Nature 521 (7553), 436.

Lee, T.C., Kashyap, R.L., Chu, C.N., 1994. Building skeleton models via 3-D medial surface axis thinning algorithms. CVGIP. Graph. Models Image Process. 56 (6), 462–478.

Lobet, G., Pages, L., Draye, X., 2011. A novel image-analysis toolbox enabling quantitative analysis of root system architecture. Plant Physiol. 157 (1), 29–39.

Lopez, L. D., Shantharaj, D., Liu, L., Bais, H., Yu, J., 2011. Robust image-based 3-d modeling of root architecture. In: Proceedings of the Computer Graphics International.

Mairhofer, S., Zappala, S., Tracy, S.R., Sturrock, C., Bennett, M., Mooney, S.J., Pridmore, T., 2012. RooTrak: automated recovery of three-dimensional plant root architecture in soil from X-ray microcomputed tomography images using visual tracking. Plant Physiol. 158 (2), 561–569.

Nair, V., Hinton, G.E., 2010. Rectified linear units improve restricted boltzmann machines. In: Proceedings of the 27th international conference on machine learning (ICML-10). pp. 807–814.

Otsu, N., 1979. A threshold selection method from gray-level histograms. IEEE Trans. Syst., Man, Cybernetics 9 (1), 62–66.

Pfeifer, J., Kirchgessner, N., Colombi, T., Walter, A., 2015. Rapid phenotyping of crop root systems in undisturbed field soils using X-ray computed tomography. Plant Methods 11 (1), 41.

Topp, C.N., Iyer-Pascuzzi, A.S., Anderson, J.T., Lee, C.R., Zurek, P.R., Symonova, O., Moore, B.T., 2013. 3D phenotyping and quantitative trait locus mapping identify core regions of the rice genome controlling root architecture. Proc. Natl. Acad. Sci. 110 (18), E1695–E1704.

Tracy, S.R., Black, C.R., Roberts, J.A., Sturrock, C., Mairhofer, S., Craigon, J., Mooney, S.J., 2012. Quantifying the impact of soil compaction on root system architecture in tomato (Solanum lycopersicum) by X-ray micro-computed tomography. Ann. Bot. 110 (2), 511–519.

Wu, A., Xu, Z., Gao, M., Buty, M., Mollura, D.J., 2016. Deep vessel tracking: A generalized probabilistic approach via deep learning. In: 2016 IEEE 13th International Symposium on IEEE Biomedical Imaging (ISBI). pp. 1363–1367.

Yazdanbakhsh, N., Fisahn, J., 2009. High throughput phenotyping of root growth dynamics, lateral root formation, root architecture and root hair development enabled by PlaRoM. Funct. Plant Biol. 36 (11), 938–946.

Zhang, W., Li, R., Deng, H., Wang, L., Lin, W., Ji, S., Shen, D., 2015. Deep convolutional neural networks for multi-modality isointense infant brain image segmentation. NeuroImage 108, 214–224.

Zheng, Y., Gu, S., Edelsbrunner, H., Tomasi, C., & Benfey, P., 2011. Detailed reconstruction of 3D plant root shape. In: 2011 IEEE International Conference on IEEE Computer Vision (ICCV). pp. 2026–2033.